published by Ural Federal University
eISSN 2411-1414; chimicatechnoacta.ru

ARTICLE
2022, vol. 9(3), No. 20229310
DOI: 10.15826/chimtech.2022.9.3.10

# Effect of cooling rate on the structure and electrochemical properties of Mn-based oxyfluorides with cation-disordered rock-salt structure

Kseniya V. Mishchenko [a], Maria A. Kirsanova [b], Arseny B. Slobodyuk [ac], Anna A. Krinitsyna [a], Nina V. Kosova [a*]

a: Institute of Solid State Chemistry and Mechanochemistry SB RAS, Novosibirsk 630128, Russia
b: Skolkovo Institute of Science and Technology, Moscow 121205, Russia
c: Institute of Chemistry FEB RAS, Vladivostok 690022, Russia
* Corresponding author: kosova@solid.nsc.ru

This paper belongs to the CTFM'22 Special Issue: https://www.kaznu.kz/en/25415/page.
Guest Editors: Prof. N. Uvarov and Prof. E. Aubakirov.

## Abstract

According to the extensive studies in the field of high-energy cathode materials for lithium-ion batteries (LIBs), Mn-based oxyfluorides $Li_{1.2}Mn_{0.6+0.5y}Nb_{0.2-0.5y}O_{2-y}F_y$ with Li-excess and cation-disordered rock-salt structure capable of reversible cationic and anionic redox reactions are among the most promising candidates. In this work, a series of Mn-based oxyfluorides with $y = 0.05$, 0.10, 0.15 were obtained using mechanochemically assisted solid-state synthesis with different cooling rates. Transmission electron microscopy, electron paramagnetic spectroscopy (EPR) and nuclear magnetic resonance spectroscopy (NMR) show that increasing the amount of fluorine promotes local ordering in crystals with the formation of isolated clusters of $Mn^{3+}$–$O^{2-}$–$Mn^{4+}$ that interrupt lithium diffusion. The occurrence of local ordering depends on the conditions of synthesis and affects electrochemistry. It was found that more clusters are formed in slowly cooled samples than in quenched ones. The best electrochemical characteristics with reversible capacity of 150 mAh·g$^{-1}$ at room temperature were demonstrated by the $Li_{1.2}Mn_{0.65}Nb_{0.15}O_{0.90}F_{0.10}$ sample obtained by quenching.

## Keywords

lithium-ion batteries
oxyfluorides
disordered rock-salt structure
local ordering
oxygen redox
$Mn^{3+}/Mn^{4+}$ redox
cyclability

Received: 24.06.22
Revised: 21.07.22
Accepted: 22.07.22
Available online: 04.08.22

## 1. Introduction

Over the past two decades, electrochemical energy storage systems have been actively introduced in a variety of fields, from portable equipment to electric vehicles and energy storage devices. With the development of new technologies, the requirements for lithium-ion batteries (LIB) are increasing, which primarily concerns specific energy. The efforts of researchers are focused on optimizing the properties of cathode materials.

In the last few years, a new class of cathode materials for LIBs has been proposed based on oxides with the disordered rock-salt structure (DRX), in which Li and transition metal (TM) ions randomly occupy octahedral sites. Until recently, these structures were excluded as possible cathode materials, since it was believed that they have a small electrochemical activity due to limited diffusion of Li$^+$. In disordered rock-salt structures, Li diffusion proceeds by hopping from one octahedral site to another octahedral site via an intermediate tetrahedral void (*o-t-o* diffusion), where *o* is an octahedron and *t* is a tetrahedron. A tetrahedral void shares faces with octahedra: one, in which there is no transition metal (0TM), another has one transition metal (1TM), or two transition metals (2TM). Further studies have shown that the excess of Li forms a percolation network consisting of 0TM tetrahedral voids, which are surrounded only by Li$^+$ ions and provide sufficient Li$^+$ mobility [1]. Highly valent transition metal ions, such as 3d Ti$^{4+}$, 4d Nb$^{5+}$ or 4d Mo$^{6+}$, are used to increase the Li$^+$ content in the structure and, as a result, specific capacity [2–4]. On the other hand, the authors [5] showed that highly valent TM are more prone to repel each other and intimately mix with Li$^+$ to maintain local electroneutrality; thus, significant Li segregation can be suppressed, which may hinder the macrodiffusion of lithium.

However, it has been shown that short-range ordering (SRO) of metal ions occurs to some extent in almost all such materials. The presence of a small number of different types of TM cations in the structure leads to the formation of SRO and, as a consequence, to a decrease in Li percolation compared to the random arrangement of metal ions [5–7]. Previously, the formation of $ONb_6$ and $OMn_1Nb_5$ octahedra, more stable than Mn-rich ones, was confirmed in DRX oxide $Li_{1.3}Nb_{0.3}Mn_{0.4}O_2$ by computational methods [8]. On the other hand, using geometrical-topological method (bond-valence site energy modeling, BVSE), and density functional theory (DFT) calculations, we demonstrated that Mn ions form $MnO_6$ clusters, which are preferably linked in dense layers in $Li_{1.3}Nb_{0.3}Mn_{0.4}O_2$, and negatively affects lithium diffusion [9]. The formation of Mn clusters was also confirmed by EPR and NMR spectroscopy [9–11].

The extra capacity of these Li-excess materials, which cannot be provided only by the redox activity of TM, is explained by the oxidation of $O^{2-}$ at high voltage [12, 13]. As a disadvantage, we can note the release of oxygen from the lattice, which is typical almost for all DRX oxides. In general, the structure of DRX oxides is stable to modifications in both the cationic and anionic sublattices. Partial substitution of oxygen with fluorine reduces irreversible O losses and improves the cyclability [2]. However, fluorine ions are more easily introduced into the anionic sublattice due to the local chemical heterogeneity caused by the presence of Li excess in the DRX structure. In this case, the degree of F doping significantly exceeds the level of surface doping, achieved in ordered layered cathode materials [13]. Fluorination of the anionic sublattice using LiF as a precursor of $F^-$ can reach ~10 at.% ($Li_{1.2}Mn_{0.625}Nb_{0.175}O_{1.95}F_{0.05}$, $Li_{1.2}Mn_{0.65}Nb_{0.15}O_{1.9}F_{0.1}$, $Li_{1.2}Mn_{0.7}Nb_{0.1}O_{1.8}F_{0.2}$) [12] when using the equilibrium solid-state method, and ~33 at.% ($Li_2Mn_{2/3}Nb_{1/3}O_2F$) when using non-equilibrium mechanochemical synthesis [4, 14, 15]. When using a fluoropolymer precursor – poly(tetrafluoroethylene), up to 12.5 at.% of fluorine can be introduced into the structure of Li–Nb–Mn–O using conventional solid-state synthesis [16]. Fluorine doping reduces the valence of the cation, which leads to an increase in the redox reservoir due to the redox processes of transition metals [4, 12]. An increase in the F content improves connectivity between Li-rich tetrahedral voids, which leads to an increase in the Li percolation. So, an important step towards sustainable cycling is to use the strategy of replacing $O^{2-}$ with $F^-$. In this case, it is possible to increase electrochemical capacity, improve the stability of cathode materials, and avoid irreversible anionic oxidation.

In addition, the release of oxygen from the lattice of oxyfluorides, observed in the differential electrochemical mass spectra, is insignificant [12, 17]. At high voltage, the release of $CO_2$ was also observed, which is assigned to interaction of carbonate solvent with highly reactive oxygen species [19]. These parasitic reactions lead to irreversible degradation of cathode material and rapid capacity loss.

In this manuscript, we study in detail the relationship between the synthesis conditions (using various cooling rates), the local structure and the electrochemical performance of the Li-rich Mn-based oxyfluoride cathode materials with the general formula $Li_{1.2}Mn_{0.6+0.5y}Nb_{0.2-0.5y}O_{2-y}F_y$ ($y$ = 0.05, 0.10, 0.15) and cation-disordered rock-salt structure.

## 2. Experimental

### 2.1. Material synthesis

Cathode materials with the general formula $Li_{1.2}Mn_{0.6+0.5y}Nb_{0.2-0.5y}O_{2-y}F_y$ ($y$ = 0.05, 0.10, and 0.15) were prepared by the mechanochemically assisted solid-state synthesis from stoichiometric reagent mixtures of LiF, $Nb_2O_5$, $Mn_2O_3$, and $Li_2CO_3$. Mechanical activation (MA) of the reagent mixtures was performed using a high-energy AGO-2 planetary mill at 600 rpm for 10 min using stainless steel jars and balls in an Ar atmosphere. The diameter of the balls was 5 mm, the volume of the jars was 125 ml, the mass ratio of the sample to the balls was 1:40. The activated mixtures were then pressed into pellets at 50 Bar and annealed at 950 °C in an Ar atmosphere for 4 h, followed by natural cooling in a furnace (hereafter, F0.05, F0.10, F0.15) or quenching (hereafter, F0.05*q*, F0.10*q*, F0.15*q*).

### 2.2. Characterization

Detailed information about the crystal and local structure, particle size and morphology were obtained using a complex of physicochemical methods. Phase composition and lattice parameters of the samples were characterized by X-ray powder diffraction (XRD) using a Bruker D8 Advance diffractometer, Cu Kα irradiation (λ = 1.54181 Å). The XRD patterns were collected over the range of 20–80° with a step of $0.02° \cdot s^{-1}$ and uptake time of 0.3–0.5 s. Structural refinement of the XRD data was carried out by the Rietveld method using the GSAS software package.

Particle size and morphology were investigated by transmission electron microscopy (TEM). The samples were prepared in air by grinding the powders in an agate mortar in acetone and depositing drops of suspension onto holey TEM grids with Lacey/Carbon support layers. Bright-field TEM (BF-TEM) images, selected area electron diffraction patterns (SAED), high angle annular dark field scanning transmission electron microscopy (HAADF-STEM) images and energy dispersive X-ray (EDX) spectra and maps were registered on an aberration-corrected Titan Themis Z transmission electron microscope equipped with a Super-X detection system and operated at 200 kV. Electron energy loss spectra (EELS) were recorded in a STEM mode with energy dispersion of 0.05 eV per channel and energy resolution of zero-loss peak of 0.85 eV using a Gatan Quantum ERS/966 P spectrometer. Oxidation state of Mn was calculated from $L_{III}/L_{II}$ line ratio according to the algorithm described by Tan et al. [20].

Electron paramagnetic resonance (EPR) spectroscopy (Adani SPINSCAN X, Belarus) was used to determine the presence of possible paramagnetic interactions in the samples. The EPR spectra were registered as the first derivative of the absorption signal within the center field of 336 mT, microwave frequency of 9415 MHz, power of 0.240 mW, and modulation frequency of 100 kHz at room temperature (25 °C) and in liquid nitrogen (–196 °C). The g-factor was established with respect to the $CuCl_2 \cdot 2H_2O$ standard. Signal intensities were normalized based on the mass of the sample.

$^7$Li MAS NMR spectra were obtained by means of an Avance AV-300 solid state Bruker spectrometer ($B_0 = 7.05T$) with a rotor synchronized Hahn echo pulse sequence using a 4 mm MAS probe at 300 K. A sample rotation frequency of 14 kHz was used for the final spectra; the separation of the sidebands from the main signal was performed using a 12 kHz frequency. The Li chemical shifts were referenced to 1 M LiCl water solution (0 ppm). $^{19}$F NMR spectra were recorded using a direct 90° pulse method of registration. The chemical shifts of $^{19}$F were referenced to $CFCl_3$ (0 ppm).

### 2.3. Electrochemical measurements

For the electrochemical testing, the as-prepared samples were mixed with 5 wt.% carbon black "P 277" from the Center of New Chemical Technologies of the Institute of Catalysis SB RAS, Omsk Branch by ball milling at 400 rpm for 2.5 minutes. To obtain working electrodes, the slurry consisting of 75 wt.% active material, 20 wt.% carbon black (in total), and 5 wt.% polyvinylidene fluoride dissolved in N-methyl-2-pyrrolidone was spread on an Al foil using a doctor blade technique and dried at 90 °C for 2 h in vacuum and then laminated. Then, discs with a diameter of 11 mm were cut out with a loading density of the active material of 2–3 mg cm$^{-2}$. The Swagelok-type cells were assembled in an argon-filled glove box (VBOX-SS 950, Vilitek, Russia) with Li metal foil as an anode. 1 M $LiPF_6$ (Sigma Aldrich, 98%) solution mixed with ethylene carbonate and dimethyl carbonate (Alfa Aesar, 99%) 1:1 by weight was used as an electrolyte, and a glass fiber filter (Whatman, Grade GF/C) was used as a separator. Cycling was performed in a galvanostatic mode at a C/40 charge/discharge rate within the voltage range of 1.5–4.8 V vs $Li/Li^+$ at room temperature using a Biologic BCS 805 battery testing system.

## 3. Results and discussion

### 3.1. Phase composition, morphology and homogeneity

As it was previously shown [14], anionic substitution in DRX without the formation of a secondary LiF phase is possible only with a fluorine content of less than 7.5 at.%. The XRD patterns of the F0.05, F0.05*q*, F0.10*q* samples obtained at different cooling rates with different amounts of $F^-$ do not contain any impurity phases (Figure 1a), while the samples with a high fluorine content ($y = 0.15$) have a very broad reflections at 23.9 (2θ), which were earlier interpreted as (101) planes of a body centered tetragonal supercell with the space group (S.g.) $I4_1/amd$ [7]. The XRD patterns of the phase pure materials were refined by the Rietveld method in the cubic S.g. *Fm*–3m (Figure 1b) with unit cell parameters given in Table 1. As can be seen, with an increase in the F content, the lattice parameters have a tendency to decrease due to the differences in ionic radii of oxygen and fluorine ($r_{O^{2-}} = 1.4$ Å, $r_{F^-} = 1.33$ Å). The average crystallite sizes (CS), determined by the XRD analysis using the Scherrer equation with the Lorentzian component of the reflection broadening (Table 1) are close to each other and are larger for the naturally cooled samples, which indicates a higher degree of crystallinity of these samples.

Since all samples were synthesized at the same temperature, we do not expect any noticeable difference in the particle sizes, which is clearly confirmed by the HAADF-STEM images (Figures 2 and S1). The particles of F0.05, F0.05*q*, F0.10*q*, and F0.15*q* have an irregular form and an average size from 0.5 to 3–5 μm (Figure S1). Individual and mixed elemental STEM-EDX maps in Figure 2 illustrate the homogeneous distribution of TM cations, which lies on the same level for all samples (Figure S2).

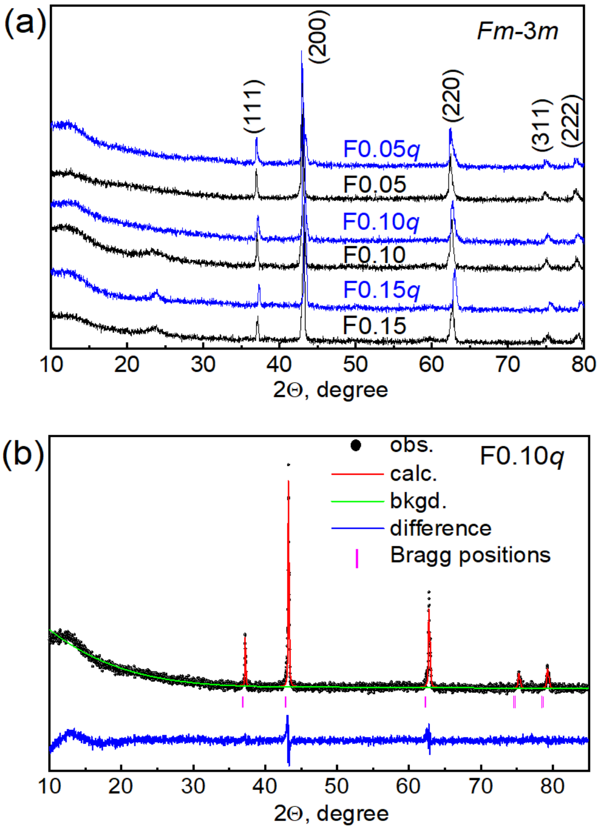

**Figure 1** Powder XRD patterns of the F0.05, F0.10, F0.15 samples obtained by natural cooling and quenching (a). Rietveld refined XRD pattern of the F0.10*q* sample based on the cubic structure with *Fm*–3*m* space group (b).

**Table 1** Rietveld refined lattice parameters and the average crystallite size (CS) of the samples obtained with natural cooling and quenching in Ar.

| Sample | F0.05 | F0.10 | F0.15 | F0.05*q* | F0.10*q* | F0.15*q* |
|---|---|---|---|---|---|---|
| a, Å | 4.1907(5) | 4.1870(5) | 4.1829(6) | 4.1843(7) | 4.1883(6) | 4.1778(8) |
| $V$, Å$^3$ | 73.60 | 73.40 | 73.19 | 73.26 | 73.47 | 72.92 |
| $R_{wp}$, % | 4.28 | 4.83 | 4.59 | 5.37 | 4.73 | 5.21 |
| GOF | 1.33 | 2.05 | 1.71 | 2.17 | 1.10 | 1.25 |
| CS, nm | 34 | 28 | 25 | 26 | 24 | 29 |

As can be seen from the EDX spectra in Figure S3, the Mn:Nb atomic ratio increases from F0.05 to F0.15*q* as expected from the nominal composition.

## 3.2. Local ordering

The [001] and [011] SAED patterns of F0.05 (Figure 3a, b) demonstrate diffuse scattering patterns typical of the F-centered cubic structure with SRO, and are very similar to those of Li–Nb–Mn–O materials [5–7]. High-resolution HAADF-STEM images show the variable intensity of atomic columns, which means that brighter columns are enriched with heavier Nb, while less intense columns contain more Mn (Figures 3c, d).

The SAED patterns and HAADF-STEM images of F0.05*q* and F0.10*q* look similar to those of F0.05 (Figure S4) and correspond to the disordered rock-salt structure with the SRO of TM cations. In the F0.15*q* sample, a higher degree of local ordering was found for all the crystals studied. The [001] and [011] SAED patterns of F0.15*q* in Figures 4a, b show a dashed scattering pattern instead of a circular one, while the [001] and [011] SAED patterns registered from another F0.15*q* crystal (Figures 4c, d) have point reflections corresponding to superstructure cubic lattices with $a_{super} = 2a_{basic}$ or $a_{super} = 4a_{basic}$ or their superposition. At the same time, the HAADF-STEM image taken from more ordered F0.15*q* crystals (Figure S4) is not distinguishable from HAADF-STEM images of other samples. Thus, we suppose that partially ordered and fully ordered domains can coexist in one crystal. Such a change in the ordering of TM in F0.15*q* in comparison with the other samples correlates with the Mn:Nb atomic ratio (Table 2) and the absolute amount of Mn in the crystal structure.

As described in Ref. [7], slow cooling during the synthesis of the $Li_{1.25}Nb_{0.25}Mn_{0.5}O_2$ oxide leads to the formation of a thermodynamically stable phase, but the short correlation length of ordering is realized in the quenched DRX oxide. With an increase in the F at.%, the Mn content also increases for charge compensation, which, in turn, can lead to the formation of Mn-enriched arrangement similar to that described in Ref. [7]. In a "high entropy" concept, the term $-T\Delta S_{mix}$ in Equation 1 is insufficient to overcome $\Delta H_{mix}$, and the structures with more favorable enthalpies are formed [21]:

$$\Delta G_{mix} = \Delta H_{mix} - T\Delta S_{mix}. \qquad (1)$$

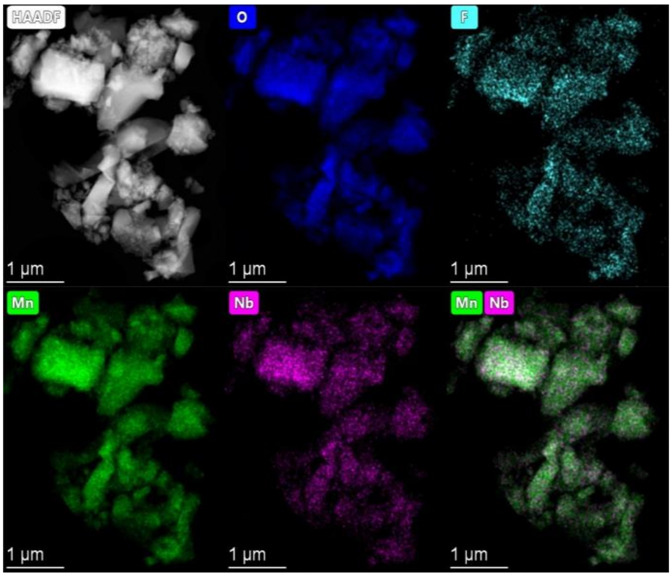

**Figure 2** HAADF-STEM image, individual EDX maps of O, F, Mn, Nb and mixed Mn/Nb compositional EDX map of the F0.05 sample.

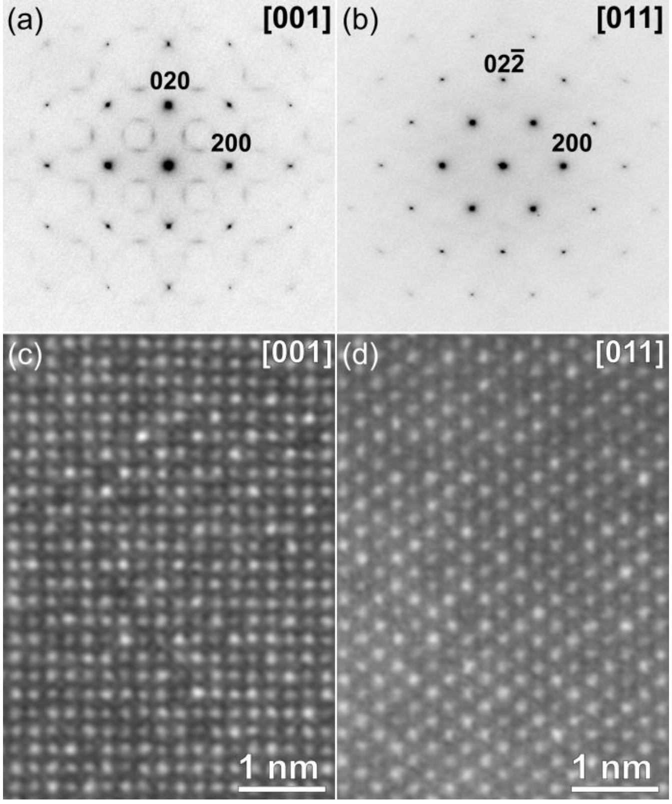

**Figure 3** [001] and [011] SAED patterns of F0.05 (a, b) indexed in the *F*-centered cubic cell and Fourier-filtered high-resolution [001] and [011] HAADF-STEM images (c, d).

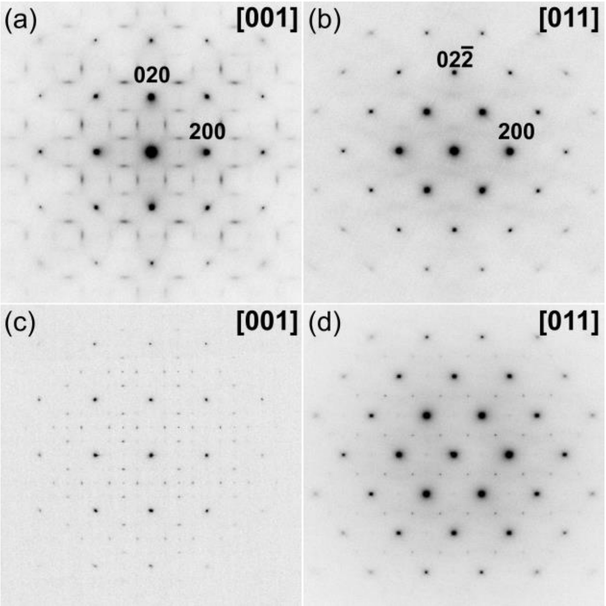

**Figure 4** [001] and [011] SAED patterns taken from two different crystals of F0.15*q* (a, b and c, d).

If we assume that the contribution of anionic sites has a negligible effect on the configuration entropy $S_{conf}$, then $S_{conf}$ as a function of a molar fraction in Equation 2 decreases and is equal to 0.88*R* (*R* is the ideal gas constant), 0.86*R*, and 0.85*R* for F0.05, F0.10, and F0.15, respectively:

$$S_{conf} = -R/2[(\sum x_i \ln x_i)_{cation} + (\sum x_i \ln x_i)_{anion}]. \qquad (2)$$

Thus, we should expect a more uniform distribution of cations for the F0.05 composition. The average oxidation state of Mn in the crystals synthesized by quenching, measured by the EELS method, is close to +3 and is slightly below +3 for the F0.05 sample (Table 2). The decrease in the state of charge can be explained by a partial reduction of Mn ions during synthesis. No noticeable disproportion between reduced and oxidized Mn states was found for these four samples. Thus, the average oxidation state of Mn is +2.90(3), +3.06(4), +2.95(6), and +3.05(3) for the F0.05, F0.05*q*, F0.10*q*, F0.15*q* samples, respectively.

Earlier, it was found that the $Li_{1.3}Nb_{0.3}Mn_{0.4}O_2$ oxide has a tendency to form the $Mn^{3+}$–O–$Mn^{4+}$ clusters [9]. On the other hand, the authors [10] revealed ferromagnetic interactions in $Li_{1.2}Ti_{0.4}Mn_{0.4}O_2$ oxide during cycling. To determine whether the ferromagnetic interactions occur in our samples or not, EPR spectra were taken both at room temperature (25 °C) and in liquid nitrogen (–196 °C).

It is known that $Mn^{3+}$ in a high spin state (electronic configuration $3d^4$, $S = 2$) has a silent EPR spectrum [10]. For all samples, the EPR signal exhibits the Lorentzian line shape with a significant broadening (Figure 5a). The line width from peak to peak is 360, 280, 269 mT for the F0.05, F0.10, F0.15 samples and 299, 293, 246 mT for the F0.05*q*, F0.10*q*, F0.15*q* samples, respectively (Figure S5). The reason for the broadening may be related to the presence of local paramagnetic clusters that are magnetically isolated from the rest of the framework by diamagnetic surroundings of $Li^+$ and $Nb^{5+}$ [11,22]. With an increase in the $F^-$ content, the estimated number of paramagnetic centers (p.c.) decreases and corresponds to 0.26, 0.14, 0.08 at.% of the initial Mn content for the F0.05, F0.10, F0.15 samples, respectively. Obviously, the decrease in signal intensity is associated with an increase in F–Mn–F bonds (more ionic), where Mn ions are more difficult to oxidize, in contrast to Mn ions with oxygen coordination [4]. The wide paramagnetic signal for F0.10, taken at –196 °C, disappears, indicating that the super-exchange interaction is not ferromagnetic (Figure 5a) [10, 23].

**Table 2** Average oxidation state of Mn calculated from EELS data and Mn:Nb atomic for the $Li_{1.2}Mn_{0.6+0.5y}Nb_{0.2-0.5y}O_{2-y}F_y$ samples.

| Sample | F0.05 | F0.05*q* | F0.10*q* | F0.15*q* |
|---|---|---|---|---|
| Average oxidation state of Mn | +2.90(3) | +3.06(4) | +2.95(6) | +3.05(3) |
| EDX Mn:Nb atomic ratio | 0.79:0.21(1) | 0.81:0.19(1) | 0.83:0.17(1) | 0.86:0.14(1) |
| Theoretical Mn:Nb atomic ratio | 0.78:0.22 | 0.78:0.22 | 0.81:0.19 | 0.84:0.16 |

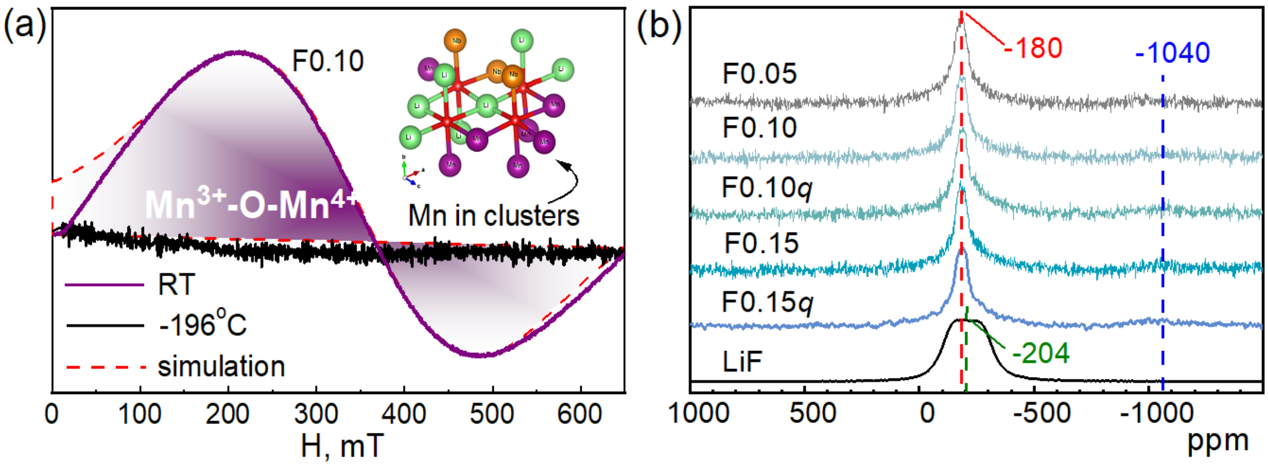

**Figure 5** EPR spectra of the F0.10 sample, recorded at 25 °C and –196 °C (a). Dotted line corresponds to the simulated spectrum. $^{19}F$ NMR spectra of the F0.05, F0.10, F0.10*q*, F0.15, and F0.15*q* samples recorded using direct 90° pulse registration method (b).

The number of p.c. in quenched samples increases with increasing Mn content. There is a superposition of two Mn states (a narrow shoulder in a wide signal) with a g-factor close to 2 (Figure S5). The amount of $Mn^{4+}$ in a diamagnetic environment ($Li^+$ or $Nb^{5+}$), calculated from the integral intensity, is less than the amount of $Mn^{4+}$ in clusters and correlates as 0.001:0.02; 0.002:0.02; 0.006:0.06 at.% for the F0.05*q*, F0.10*q*, F0.15*q* samples, respectively. Summarizing, we can say that the amount of p.c. and $Mn^{3+}$ ions in clusters is significantly less in quenched samples due to the possible formation of oxygen vacancies [24]. With an increase in the Mn or F content, the formation of more $Mn^{3+}$–O–$Mn^{4+}$ clusters and $Mn^{4+}$ ions in a diamagnetic environment is observed, which indicates that the more $Li^+$ accumulates around $F^-$ with formation of sublattice populated with Li-rich medium, which also corresponds to the XRD data for the F0.10*q* and F0.15*q* samples (Figure 1).

To get more information about the local lithium environment, MAS NMR studies were conducted. $^7$Li MAS NMR spectra of the F0.05, F0.10, F0.15, F0.10*q*, F0.15*q* samples in Figure S6 consist of a wide asymmetric background (*p*1) and an asymmetric narrow line due to magic angle spinning along with its spinning sidebands, which can be deconvoluted into the peaks *p*2 and *p*3 (Table 3).

Lithium, being in a paramagnetic $Mn^{3+}$ environment, experiences a strong dipole-dipole interaction, which leads to the appearance of a number of signals shifted to a weaker and stronger magnetic field. This also leads to a broadening of the NMR signal [10]. As can be seen from Table 3, the position of the wide component (δ1) and its intensity are associated with the Mn content. With an increase in the Mn content, the average shift of δ1 and the gravity center position *M*1 are directed toward a weak magnetic field. These averaged shifts lie far beyond the range of lithium chemical shift for diamagnetic compounds and are the result of contact Fermi interaction with $Mn^{3+}$ centers. It can be noted, that the differences in *M*1 between the samples prepared with and without quenching are quite small. The large value of *M*1 observed for the F0.15*q* sample may be due to increased 90° Li–O–Mn interaction [25]. Taking into account the view of the SAED patterns for various crystals (Figure 4), the low-field shift can be related to the Mn clusterization taking place for the quenched F0.15*q* sample.

On the enlarged fragment of the MAS component (Figure S6), it is possible to notice the asymmetry of the signal, which can be explained by the interaction of the quadrupolar $^7$Li nuclei with the electric field gradient. The small quadrupolar moment of the nucleus and the cubic symmetry of the structure lead us to the conclusion that the MAS peaks should be divided into two overlapping lines. The lines narrowed with MAS correspond to lithium sites adjacent only to the diamagnetic ($Nb^{5+}$) nearest neighbors. The positions and intensities of the components, which for the MAS lines include the intensities of 12 corresponding spinning sidebands, are shown in Table 3. There is some variation in the positions of the MAS components that could be related to the volumetric susceptibility of the samples.

$^{19}$F NMR data confirm the presence of the interaction between oxides and LiF (Figure 5b). All studied samples have similar spectra with the shape and shift of the dominant signal differing from those of LiF. The half-width of the spectra for the studied samples is ~20 kHz, and the shift is about −180 ppm, while for LiF, these values are 64 kHz and −204 ppm, respectively. The spectra of the studied materials also contain a wide low-intensity signal of about −1040 ppm.

In the case of fluorine coordinated by $Mn^{3+}$ ion, a strong dipole-dipole interaction of order of megahertz exists between unpaired electrons of the $Mn^{3+}$ ion and $^{19}$F nucleus. Therefore, only fluorine in a diamagnetic environment is expected to give rise to an NMR signal. The shift of −180 ppm falls within a diamagnetic chemical shift range and may correspond to bridged axial fluorine in coordination of Nb [26]. The non-bridged equatorial fluorine resonating in the positive region of chemical shifts is not visible in the spectra. The shape and the half-width of the spectra are determined by the interaction with lithium ions, while the main contribution of LiF is due to dipole-dipole interactions between fluorine nuclei. The signal at −1040 ppm probably comes from the similar environment, where the next nearest neighbor of fluorine is the $Mn^{3+}$ ion and the unpaired electron density is transferred to the 2s orbitals of fluorine, which leads to a contact shift.

### 3.3. Electrochemistry

The electrochemical properties of the samples were studied by galvanostatic cycling (Figures 6a and S7). Theoretical capacities based on the Li content are 353, 356, and 359 mAh·g$^{-1}$ for F0.05, F0.10, and F0.15, respectively, of which 184, 193, and 202 mAh·g$^{-1}$ comes from the $Mn^{3+}/Mn^{4+}$ redox couple. The value of the experimental specific capacity for the first charge for all samples exceeds the capacity calculated for the $Mn^{3+}/Mn^{4+}$ redox couple, which indicates the participation of the $O^{2-}/O^-$ couple in the cycling process. For all samples, an irreversible drop of the specific capacity is observed during the first cycle.

**Table 3** $^7$Li NMR peak shifts and intensities.

| **Sample** | **$\delta_1$[a], ppm** | **$I_1$[a], %** | **$\delta_2$, ppm** | **$I_2$, %** | **$\delta_3$, ppm** | **$I_3$, %** | **Err., %** | **$M_1$[b]** |
|---|---|---|---|---|---|---|---|---|
| F0.05 | 245 | 94 | 9 | 2 | −2 | 3 | 3.0 | 241 |
| F0.10 | 268 | 96 | 9 | 1 | −1 | 3 | 3.3 | 266 |
| F0.10q | 263 | 96 | 8 | 1 | −1 | 3 | 2.8 | 239 |
| F0.15 | 308 | 95 | 6 | 1 | −2 | 3 | 3.1 | 294 |
| F0.15q | 321 | 96 | 8 | 1 | −2 | 3 | 2.7 | 309 |

[a] $\delta_n$, $I_n$: position and integrated intensity of the component $p_n$.

[b] $M_1$: center of gravity of the spectrum.

The difference in charge and discharge capacity values is usually associated with the formation of a cathode-electrolyte interface (CEI) on the surface of electrode along with $Li^+$ deintercalation. The differential curves $dQ/dV$ of the first charge show three oxidation peaks at 3.6, 4.4, and 4.6 V, which are related to the oxidation reaction of $Mn^{3+}$ and $O^{2-}$ ions (Figures 6b and S7). The third oxidation peak on the differential curves is observed at ~4.8 V (Figures 6b and S7), which is similar to that observed in Li–Nb(Ti)–Mn–O(F) systems [27, 28]. This may be a result of parasitic side reactions of highly reactive oxidized oxygen species with the electrolyte or irreversible release of $O_2$ gas from the lattice at high voltage [12, 16, 18]. On the other hand, as mentioned in Ref. [28], the presence of highly valent transition metal ions (such as $Mn^{4+}$) has a catalytic effect on the position of the peak of side reactions during the first charge. Among all prepared oxyfluorides, the most intense oxidation peak is observed for the F0.05 sample, where the number of p.c. ($Mn^{4+}$) is maximal.

Comparing the electrochemical behavior of all the samples, the highest contribution of the $O^{2-}/O^-$ redox couple in specific capacity on the second cycle is observed for the F0.10 and F0.10*q* (Figures 6 and S7). This can be explained by the optimal content of F, which stabilizes the $O^{2-}/O^-$ redox reaction [3, 12, 16]. Moreover, the quenched F0.10*q* sample demonstrates contribution of both $Mn^{3+}/Mn^{4+}$ and $O^{2-}/O^-$ redox couples with discharge capacity of about 150 $mAh \cdot g^{-1}$ after 10 cycles (Figure 7). On the other hand, the best capacity retention after 10 cycles is observed for the F0.15 and F0.15*q* samples, which can be explained by the maximum Mn content along with the less contribution of $O^{2-}/O^-$ redox couple. The existence of large amount of Nb in the DRX structure contributes to an increase in the number of 180° Li–O–Li bonds [29, 30] necessary for the activation of the $O^{2-}/O^-$ redox couple. This leads to oxidation of oxygen $O^-$ ions that are inherently unstable and release in the form of $O_2$ from the lattice. Therefore, the reason of the capacity loss is the TM migration and densification of the crystal lattice as a result of $O_2$ loss [10, 16]. The second reason for the capacity loss is the formation of isolated 0TM tetrahedra due to the accumulation of $Li^+$ around the $F^-$ ion. These processes are irreversible and interrupt lithium diffusion. Thus, the optimal electrochemical properties can be achieved by combining the required amount of $d^0$ TM and $F^-$ ions.

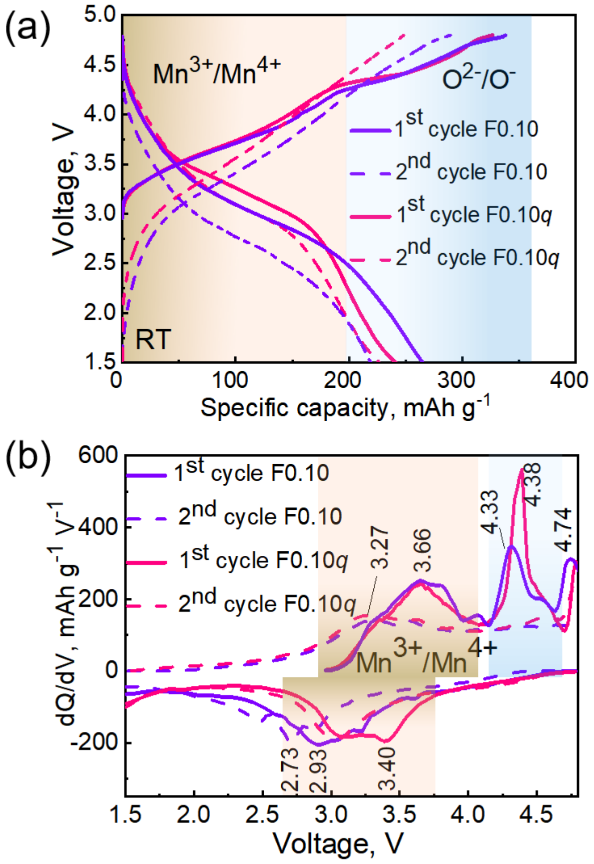

**Figure 6** Charge-discharge curves of the F0.10 and F0.10*q* samples, cycled at the C/40 charge/discharge rate within the voltage range of 1.5–4.8 V at RT (a) and corresponding $dQ/dV$ curves (b).

## 4. Conclusions

We described for the first time the effect of the cooling rate on the crystal and local structure of $Li_{1.2}Mn_{0.6+0.5y}Nb_{0.2-0.5y}O_{2-y}F_y$ ($y$ = 0.05, 0.10, 0.15) oxyfluorides. It was shown that increasing the cooling rate can stabilize the disorder, thereby suppressing local ordering and superstructure formation. This was also confirmed by EPR and NMR spectroscopy, which show a smaller number of $Mn^{3+}$–$O^{2-}$–$Mn^{4+}$ clusters in the quenched samples. The minimum amount of the paramagnetic clusters was observed for the $Li_{1.2}Mn_{0.625}Nb_{0.175}O_{0.95}F_{0.05}$ sample. The fluorine content influences the local ordering of $Mn^{3+}$ ions: with an increase in the F content, the amount of paramagnetic centers decreases, and the minimum amount of them is observed for the $Li_{1.2}Mn_{0.675}Nb_{0.125}O_{0.85}F_{0.15}$ sample. This effect may be associated with the interruption of magnetic exchange interactions in Mn clusters by replacing $O^{2-}$ ions with $F^-$.

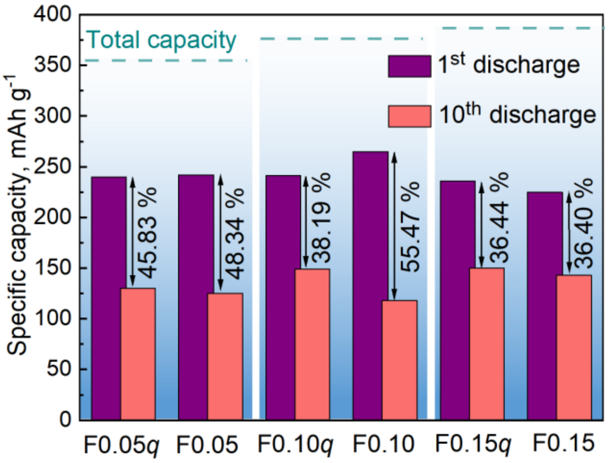

**Figure 7** The loss of discharge capacity after 10 cycles for all samples. The dotted lines indicate the total theoretical capacity.

It was established that the cooling rate influences the electrochemical properties of the samples: the capacity retention is higher for the samples obtained by quenching. In addition, the fluorine content affects the stability of the $O^{2-}/O^{-}$ redox couple and its contribution to the specific capacity. Despite the greater contribution of the $O^{2-}/O^{-}$ redox couple to the capacity of the $Li_{1.2}Mn_{0.625}Nb_{0.175}O_{0.95}F_{0.05}$ sample, this sample suffers from irreversible oxygen loss. Stable contribution of both $Mn^{3+}/Mn^{4+}$ and $O^{2-}/O^{-}$ redox couples in specific capacity is characteristic of the $Li_{1.2}Mn_{0.65}Nb_{0.15}O_{0.90}F_{0.10}$ sample. Thus, the selection of the optimal fluorine content and cooling rate leads to the production of cathode materials with the best electrochemical properties.

## Supplementary materials

This manuscript contains supplementary materials, which are available online.

## Funding

This work was supported by the Russian Science Foundation (grant no. 21-73-20064), https://www.rscf.ru/en.

RSF Russian Science Foundation

## Acknowledgments

The authors would like to acknowledge Dr. Anna Matveeva at the Institute of Solid State Chemistry and Mechanochemistry SB RAS for the assistance in registering the EPR spectra.

## Author contributions

Conceptualization: N.V.K.
Data curation: K.V.M., M.A.K., A.B.S., A.A.K.
Formal Analysis: K.V.M.
Investigation: K.V.M., M.A.K., A.B.S.
Methodology: K.V.M., N.V.K.
Project administration: N.V.K.
Supervision: N.V.K.
Validation: N.V.K.
Visualization: K.V.M.
Writing – original draft: K.V.M.
Writing – review & editing: N.V.K.
Funding acquisition: N.V.K.

## Conflict of interest

The authors declare no conflict of interest.

## Additional information

Author IDs:
Kseniya V. Mishchenko, Scopus ID 55226355900;
Maria A. Kirsanova, Scopus ID 57189519143;
Arseny B. Slobodyuk, Scopus ID 9632643200;
Nina V. Kosova, Scopus ID 7003555655.

Websites:
Institute of Solid State Chemistry and Mechanochemistry SB RAS, http://www.solid.nsc.ru/;
Skolkovo Institute of Science and Technology, https://www.skoltech.ru/en;
Institute of Chemistry FEB RAS, http://www.ich.dvo.ru/.

## References

1. Lee J, Urban A, Li X, Su D, Hautier G, Ceder G. Unlocking the potential of cation-disordered oxides for rechargeable lithium batteries. Sci. 2014;343:519–522. doi:10.1126/science.1246432
2. Yabuuchi N. Material design concept of lithium-excess electrode materials with rocksalt-related structures for rechargeable non-aqueous batteries. Chem Rec. 2019;19:690–707. doi:10.1002/tcr.201800089
3. Lun Z, Ouyang B, Kwon DH, Ha Y, Foley EE, Huang TY, Cai Z, Kim H, Balasubramanian M, Sun Y, Huang J, Tian Y, Kim H, McCloskey BD, Yang W, Clément RJ, Ji H, Ceder G. Cation-disordered rock-salt-type high-entropy cathodes for Li-ion batteries. Nat Mater. 2021;20:214–221. doi:10.1038/s41563-020-00816-0
4. Lee J, Kitchaev DA, Kwon DH. Lee CW, Papp JK, Liu YS, Lun Z, Clément RJ, Shi T, McCloskey BD, Guo J, Balasubramanian M, Ceder G. Reversible $Mn^{2+}/Mn^{4+}$ double redox in lithium-excess cathode materials. Nat. 2018;556:185–190. doi:10.1038/s41586-018-0015-4
5. Ji H, Urban A, Kitchaev DA, Kwon DH, Artrith N, Ophus C, Huang W, Cai Z, Shi T, Kim JC, Kim H, Ceder G. Hidden structural and chemical order controls lithium transport in cation-disordered oxides for rechargeable batteries. Nat Commun. 2019;10:592–600. doi:10.1038/s41467-019-08490-w
6. Ouyang B, Artrith N, Lun Z, Jadidi Z, Kitchaev DA, Ji H, Urban A, Ceder G. Effect of fluorination on lithium transport and short-range order in disordered-rocksalt-type lithium-ion battery cathodes. Adv Energy Mater. 2020;1903240. doi:10.1002/aenm.201903240
7. Jones MA, Reeves PJ, Seymour ID, Cliffe MJ, Dutton SE, Grey CP. Short-range ordering in a battery electrode, the 'cation-disordered' rocksalt $Li_{1.25}Nb_{0.25}Mn_{0.5}O_2$. Chem Commun. 2019;55:9027–9030. doi:10.1039/c9cc04250d
8. Kan WH, Deng B, Xu Y, Shukla AK, Bo T, Zhang S, Liu J, Pianetta P, Wang BT, Liu Y, Chen G. Understanding the effect of local short-range ordering on lithium diffusion in $Li_{1.3}Nb_{0.3}Mn_{0.4}O_2$ single-crystal cathode. Chem. 2018;4:2108–2123. doi:10.1016/j.chempr.2018.05.008
9. Semykina DO, Morkhova YeA, Kabanov AA, Mishchenko KV, Slobodyuk AB, Kirsanova MA, Podgornova OA, Shindrov AA, Okhotnikov KS, Kosova NV. Effect of transition metal cations on the local structure and lithium transport in disordered rock-salt oxides. Phys Chem Chem Phys. 2022;24:5823–5832. doi:10.1039/D1CP04993C
10. Geng F, Hu B, Li C, Zhao C, Lafon O, Trébosc J, Amoureux JP, Shen M, Hu B. Anionic redox reactions and structural degradation in a cation-disordered rock-salt $Li_{1.2}Ti_{0.4}Mn_{0.4}O_2$ Cathode material revealed by solid-state NMR and EPR. J Mater Chem A. 2020;8:16515–16526. doi:10.1039/d0ta03358h
11. Stoyanova R, Gorova M, Zhecheva E. EPR of Mn4+ in spinels $Li_{1+x}Mn_{2-x}O_4$ with $0 \le x \le 0.1$. J Phys Chem Solids. 2000;61(4):609–614. doi:10.1016/S0022-3697(99)00244-9
12. Lun Z, Ouyang B, Kitchaev DA, Clément RJ, Papp JK, Balasubramanian M, Tian Y, Lei T, Shi T, McCloskey BD, Lee

J, Ceder G. Improved cycling performance of Li-excess cation-disordered cathode materials upon fluorine substitution. Adv Energy Mater. 2019;9:1802959. doi:10.1002/aenm.201802959

13. Croguennec L, Bains J, Ménétrier M, Flambard A, Bekaert E, Jordy C, Biensan P, Delmas C. Synthesis of "$Li_{1.1}(Ni_{0.425}Mn_{0.425}Co_{0.15})_{0.9}O_{1.8}F_{0.2}$" materials by different routes: is there fluorine substitution for oxygen? J Electrochem Soc. 2009;156:A349. doi:10.1149/1.3080659
14. Lun Z, Ouyang B, Cai Z, Cle´ment RJ, Kwon DH, Huang J, Papp JK, Balasubramanian M, Tian Y, McCloskey BD, Ji H, Kim H, Kitchaev DA, Ceder G. Design principles for high-capacity Mn-based cation-disordered rocksalt cathodes. Chem. 2020;6:153–168. doi:10.1016/j.chempr.2019.10.001
15. Kitchaev DA, Lun Z, Richards WD, Ji H, Clément RJ, Balasubramanian M, Kwon DH, Dai K, Papp JK, Lei T, McCloskey BD, Yang W, Lee J, Ceder G. Design principles for high transition metal capacity in disordered rocksalt Li-ion cathodes. Energy Environ Sci. 2018;11:2159–2171. doi:10.1039/C8EE00816G
16. Ahn J, Chen D, Chen G. A fluorination method for improving cation-disordered rocksalt cathode performance. Adv Energy Mater. 2020;10:2001671. doi:10.1002/aenm.202001671
17. Crafton MJ, Yue Y, Huang TY, Tong W, McCloskey BD. Anion reactivity in cation-disordered rocksalt cathode materials: the influence of fluorine substitution. Adv Energy Mater. 2020;10:2001500. doi:10.1002/aenm.202001500
18. Renfrew SE, McCloskey BD. Residual lithium carbonate predominantly accounts for first cycle $CO_2$ and CO outgassing of Li-stoichiometric and Li-rich layered transition metal oxides. J Am Chem Soc. 2017;139:17853–17860. doi:10.1021/jacs.7b08461
19. Freunberger SA, Chen Y, Peng, Z, Griffin JM, Hardwick LJ, Barde F, Novak P, Bruce PG. Reactions in the rechargeable Lithium-$O_2$ battery with alkyl carbonate electrolytes. J Am Chem Soc. 2011;133:8040–8047. doi:10.1021/ja2021747
20. Tan H, Verbeeck J, Abakumov A, Tendeloo GV. Oxidation state and chemical shift investigation in transition metal oxides by EELS. Ultramicroscop. 2012;116:24–33. doi:10.1016/j.ultramic.2012.03.002
21. Lin L, Wang K, Azmi R, Wang J, Sarkar A, Botros M, Najib S, Cui Y, Stenzel D, Sukkurji PA, Wang Q, Hahn H, Schweidler S, Breitung B. Mechanochemical synthesis: route to novel rock-salt structured high-entropy oxides and oxyfluorides. J Mater Sci. 2020;55:16879–16889. doi:10.1007/s10853-020-05183-4
22. Stoyanova RK, Zhecheva EN, Gorova MY. EPR evidence on short-range Co/Mn order in $LiCoMnO_4$ spinels. J Mater Chem. 2000;10:1377–1381. doi:10.1039/A909066E
23. Julien C, Gendron F, Ziolkiewicz S, Nazri GA. Electrical and ESR studies of lithium manganese oxide spinels. Mat Res Soc Symp Proc. 1998;548:187–195. doi:10.1557/PROC-548-187
24. Ivakin YD, Danchevskaya MN, Murav'eva GP. State of manganese ions in the structure of corundum synthesized in supercritical water fluid. Moscow Univ Chem Bull. 2011;66(3):151–158. doi:10.3103/S0027131411030060
25. Lee YJ, Wang F, Grey CP. 6Li and 7Li MAS NMR studies of lithium manganate cathode materials. J Am Chem Soc. 1998;120(48):12601–12613. doi:10.1021/ja9817794
26. Du LS, Schurko RW, Kim N, Grey CP. Solid-state 93Nb, 19F, and 113Cd nuclear magnetic resonance study of niobium oxyfluorides: characterization of local distortions and oxygen/fluorine ordering. J Phys Chem A. 2002;106:7876–7886. doi:10.1021/jp020457q
27. Zhou K, Zheng S, Ren F, Wu J, Liu H, Luo M, Liu X, Xiang Y, Zhang C, Yang W, He L, Yang Y. Fluorination effect for stabilizing cationic and anionic redox activities in cation-disordered cathode materials. Energy Storage Mater. 2020;32:234–243. doi:10.1016/j.ensm.2020.07.012.
28. Kan WH, Chen D, Papp JK, Shukla AK, Huq A, Brown CM, McCloskey BD, Chen G. Unravelling solid-state redox chemistry in $Li_{1.3}Nb_{0.3}Mn_{0.4}O_2$ single-crystal cathode material. Chem Mater. 2018;30:1655–1666. doi:10.1021/acs.chemmater.7b05036
29. Chen D, Wu J, Papp JK, McCloskey B, Chen G. Role of redox-inactive transition-metals in the behavior of cation-disordered rocksalt cathodes. Small. 2020;16:173–177. doi:10.1002/smll.202000656
30. Clement R, Lun Z, Ceder G. Cation-disordered rocksalt transition metal oxides and oxyfluorides for high energy lithium-ion cathodes. Energy Environ Sci. 2020;1:345–373. doi:10.1039/C9EE02803J